Nonlinear Dyn
https://doi.org/10.1007/s11071-025-10989-5

RESEARCH

Unstable limit cycle estimation from small perturbations: a minimal-data-driven approach

Giuseppe Habib

Received: 13 November 2024 / Accepted: 9 February 2025

Abstract While stable solutions of dynamical systems are generally regarded as more significant than unstable ones, the latter play a crucial role in the dynamical integrity of stable steady-states. In fact, the boundaries of basins of attraction are often formed by unstable saddle-type solutions and their stable manifolds. This study proposes a method for estimating unstable limit cycles surrounding stable equilibrium points. The method leverages the shape of trajectories converging towards the equilibrium. Trajectories from small perturbations near the equilibrium state are sufficient to provide an acceptable estimate of the unstable limit cycle. No mathematical model of the system dynamics is required for the computation, which relies on just a single trajectory in the phase space. Consequently, the method is computationally efficient and can potentially be implemented in real-world structures.

Keywords Unstable limit cycle · Bifurcation forecasting · Global dynamics · Data-driven · Model-free · Transient dynamics

1 Introduction

Dynamical integrity quantifies the robustness of a system's attractors against external perturbations. In most practical cases, dynamical integrity is bounded, meaning that if a system experiences a sufficiently large perturbation from a stable steady state, it will diverge from that state. In such cases, the solution is said to be locally stable. Conversely, if the dynamical integrity is unbounded, the solution is globally stable.

This issue arises in many engineering applications and can, at times, lead to serious accidents. Examples include machining processes [1,2], flutter instability [3,4], turbulent and shear flows [5,6], pressure relief valves [7], wheel shimmy [8–10], robot control [11–13], break squeal [14,15], traffic jams [16,17], and electric blackouts [18,19], to name a few.

Dynamical integrity can be studied via their basin of attraction. The basin of attraction of a solution is the region of the phase space from which trajectories will converge to the solution.

Several methods exist to compute a solution's basin of attraction. Arguably the most effective numerical technique is the cell-mapping method, developed by Hsu in 1980 [20]. However, it suffers from memory limitations for medium- or large-scale dynamical systems and is complex to implement. Analytical methods based on Lyapunov functions can identify subsets of the basin of attraction; however, general techniques for their computation are not easily available and they often yield too conservative results [21]. Recently, methods

G. Habib
Department of Applied Mechanics, Faculty of Mechanical Engineering, Budapest University of Technology and Economics, Budapest Műegyetem rkp. 3., 1111, Hungary

G. Habib (✉)
MTA-BME Lendület "Momentum" Global Dynamics Research Group, Budapest University of Technology and Economics, Budapest Műegyetem rkp. 3., 1111, Hungary
e-mail: habib@mm.bme.hu

have been developed to quickly estimate a solution's dynamical integrity without computing the basin of attraction [22,23], but they also face challenges for large dynamical systems.

For real systems lacking an available mathematical model, computing basins of attraction is highly challenging, with only a few studies addressing this issue [24–26].

In most studies on nonlinear dynamics, only stable steady-state solutions are considered practically relevant since unstable ones are rarely realized in practice. However, unstable solutions play a crucial role in structuring the basins of attraction of stable solutions. Unstable saddle-type solutions typically lie on the boundary between basins of attraction, and their attractive manifolds define these boundaries. Because of these properties, unstable solutions are crucial to a system's dynamical integrity. Specifically, in two-dimensional systems, an equilibrium's basin of attraction is often completely defined by an unstable limit cycle (ULC). This occurs in systems where effective damping becomes negative above a certain amplitude of oscillations, typically leading to the formation of an unstable limit cycle [27]. In higher-dimensional systems, the ULC defines only a line on the boundary of the basin of attraction, yet a strong connection often exists between the equilibrium's dynamical integrity and the size of the ULC. Thus, identifying ULCs offers valuable insights into dynamical integrity.

However, ULCs are relatively difficult to identify. In some cases, they can be found analytically, or numerically through shooting or collocation methods [28], for example. They can be identified via backwards time integration in some very special cases, but their identification in experiments is particularly challenging.

The recent emergence of experimental continuation is worth noting, which consists of experimentally tracking steady-state solutions of nonlinear dynamical systems, including unstable branches [29,30]. This method uses feedback control to stabilize otherwise unstable solutions. The unstable solution is then identified by finding the conditions under which the system is in a steady state with minimal control effort [31]. A review on this topic is available in [32]. Although this method has been successfully applied to various engineering systems [33], it has the notable drawback of requiring substantial hardware resources for feedback control.

This study aims to address this gap by developing a method to estimate ULCs directly from a system's time series, without requiring specific initial conditions, feedback control, or a mathematical model for the system dynamics. The developed method leverages the so-called critical slowing down [34], i.e., the increased relaxation time of a dynamical system near a steady-state solution, which also occurs close to ULCs.

This effect has already been exploited in a series of studies by Epureano and collaborators. Their method, as presented in the initial study [35], can forecast Andronov-Hopf bifurcations and the emerging branch of periodic solutions using trajectories computed in the pre-bifurcation parameter space. By analyzing the differential amplitude-dependent decay velocity of two or more trajectories, one can estimate where the critical zero decay occurs. The branch of periodic solutions is estimated to be approximately where the decay is zero. The method has since been further refined and tested on various systems, including aeroelastic flutter [36–39], parametrically excited systems [40], and traffic jams [41]. Recently, the author of this study developed a similar algorithm specifically for identifying fold bifurcations, which typically mark regions in the parameter space where a solution is only locally stable [42]. This method was experimentally validated on a towed wheel undergoing shimmy oscillations [43].

These methods, which have proven to be highly effective, exploit the differential behavior of time series for parameter value variations to estimate where critical slowing down will occur. As such, they require large-amplitude initial conditions to cover the full amplitude range of interest. This poses a significant limitation for real-world applications, where imposing large initial conditions is often unfeasible. Additionally, in real applications, it might be impractical to modify a parameter value in a controlled manner for such estimations.

Recognizing these limitations, this study proposes a different approach to critical slowing down. Here, the critical slowing down is estimated not in the parameter space but in the phase space. In practice, this approach uses time series with relatively small initial conditions and a single set of parameter values to estimate large-amplitude unstable periodic solutions where critical slowing down occurs.

The fundamental working principle of the method is discussed in Sect. 2. Section 3 explains the algorithm in detail. The method is then tested on three systems presenting very different challenges. Namely, the mass-on-moving-belt system, which presents non-smoothness (Sect. 4), a time-delayed mathematical model for turning machining dynamics (Sect. 5), and a pitch-and-plunge wing profile undergoing flutter instability, where the challenge lies in the presence of multiple degrees of freedom (DoF) (Sect. 6). Concluding remarks are provided in Sect. 7.

2 Fundamental idea

Let us first consider a slightly damped, unforced linear oscillator, such as the classical spring-mass-damper system. For any perturbation from the trivial solution, the system oscillates with decreasing amplitude. The amplitude decrement is well described by the logarithmic decrement Λ, which is defined as

$$\Lambda = \frac{A_i}{A_{i+1}}, \tag{1}$$

where A_i is the oscillation amplitude of the i^{th} peak. For a linear system, Λ is constant, and its value is directly related to the system's damping ratio.

Now, consider a single-DoF smooth nonlinear system having a stable equilibrium surrounded by a ULC, as illustrated in Fig. 1a.

The limit cycle is a steady-state solution of the system. Accordingly, despite being unstable, a trajectory passing close to it in the phase space moves away relatively slowly. This phenomenon, known as critical slowing down [34], refers to the tendency of a system's dynamics to slow down near steady-state solutions, regardless of their stability. In this context, the system's velocity reflects how quickly it diverges from or converges toward a solution.

Consider a trajectory starting near the unstable limit cycle and converging toward the trivial solution. Unlike in the linear case, the logarithmic decrement Λ will no longer remain constant. It will start small near the ULC and increase as the system approaches equilibrium. If the trajectory begins infinitesimally close to the unstable solution, the logarithmic decrement will start from almost zero. If the initial condition lies inside the ULC, oscillation amplitude will decrease, and Λ will increase. Conversely, if the initial condition is outside the ULC, the amplitude will grow, and the logarithmic decrement will be negative and further decrease. Graphically, this behavior appears as a curve intersecting the zero axis in correspondence with the amplitude of the ULC. This phenomenon is illustrated in Fig. 1c.

By perturbing the system from equilibrium, the upper part of the curve marking the trend of the logarithmic decrement can be calculated. If the logarithmic decrement trend is sufficiently regular and can be approximated by a polynomial curve, then its intersection with the zero axis can be estimated, as discussed below in Sect. 3. Although the method is simpler for a single-DoF system, it can also be applied to larger systems, as explained in Sects. 3.3 and demonstrated in Sect. 6. The formalization of this ULC estimation method is provided in Sect. 3.

3 Unstable limit cycle estimation

3.1 Single-DoF systems

Consider a single-DoF system with a stable trivial solution and a ULC. For illustration, we examine a specific system: an oscillator with nonlinear damping characteristics, whose dynamics is governed by the differential equation

$$\ddot{x} + x + c_1\dot{x} - c_3\dot{x}^3\left(1 - \dot{x}^2\right) = 0, \tag{2}$$

where x is the state variable, c_1 the linear damping coefficient, and c_3 the nonlinear damping coefficient, governing third- and fifth-order terms. This system was thoroughly studied in [27]. For $c_1 > 0$, the trivial solution is always stable. However, while for $c_3 < c_3^* = 40c_1/9$ it is also globally stable, for $c_3 > c_3^*$ it coexists with a stable and an unstable limit cycle. The unstable limit cycle marks the boundary between the basins of attraction of the two stable solutions. At $c_3 = c_3^*$, the system undergoes a fold bifurcation, where the stable and unstable solution branches merge. Figure 2a illustrates the corresponding bifurcation diagram. In this analysis, we focus on the parameter range $c_3 > c_3^*$, where multiple solutions coexist. Without loss of generality, we fix c_1 at 0.1.

A small perturbation is applied, moving the system away from its trivial equilibrium, but within the basin of attraction of the trivial solution, i.e., inside the region bounded by the ULC. Time series and phase portrait of the ensuing dynamics are depicted in Fig. 2b and c. The peaks of the time series in Fig. 2b correspond to the intersection of the trajectory with the $\dot{x} = 0$ axis, marked by magenta dots in Fig. 2c. The first four peaks are considered, and the logarithmic decrement between

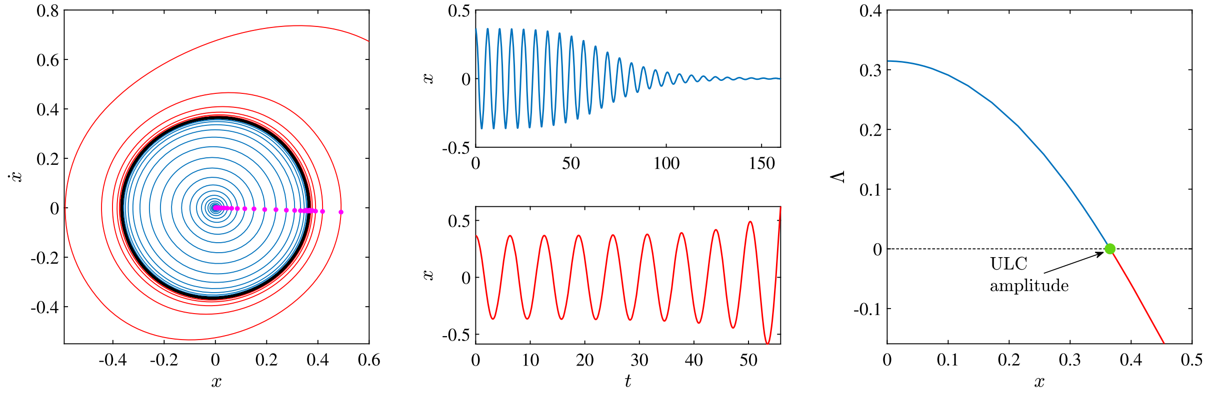

(a) (b) (c)

Fig. 1 **a** Phase portrait of a system having a stable trivial solution and a ULC (black circle); blue curve: trajectory converging to the equilibrium; red curve: trajectory diverging from it; magenta dots: intersections of trajectories with the positive zero semi-axis. **b** Time series either converging towards a stable equilibrium (top), or diverging from it (bottom). **c** Logarithmic decrement computed for each peak of the trajectories; blue curve: converging trajectory, red curve: diverging trajectory; green dot: amplitude of the ULC. (Color figure online)

consecutive peaks is calculated:

$$\Lambda_i = \frac{A_i}{A_{i+1}}. \tag{3}$$

The values of Λ_i are then paired with the average amplitudes of the corresponding peaks to obtain three couple of points:

$$\left(\frac{A_i + A_{i+1}}{2}, \Lambda_i\right), \tag{4}$$

as depicted in Fig. 2d (magenta dots). Only the first three points encountered are used since they provide the best estimation because they are the closest to the ULC.

Next, a quadratic polynomial is fitted through the three points (black curve in Fig. 2d), and its intersection with the $\Lambda = 0$ axis is calculated. The intersection gives the estimated ULC amplitude (green dot in Fig. 2d). We note that another polynomial order could be used to estimate the intersection with the $\Lambda = 0$ axis, as discussed below.

To estimate the entire ULC, not just its intersection with the $\dot{x} = 0$ axis, the procedure can then be repeated for various Poincaré sections of the phase space, each passing through zero and forming a different angle α with respect to the $\dot{x} = 0$ axis, as illustrated in Fig. 2c. For each Poincaré section, the first four intersections of the trajectory are treated in the same manner as the peaks A_i, allowing for estimation of the ULC amplitude on that section. If the angle α spans 2π radiants, the entire limit cycle can be estimated. Unusual ULC shapes, involving multiple crossing of a Poincaré section in a single loop, can cause the procedure to fail. However, such cases are rare, making this limitation not critical. Moreover, coordinate transformations can help mitigate this issue.

Figure 2e compares estimated ULCs with the exact one for different perturbation amplitudes. Remarkably, even small perturbations provide accurate ULC estimates, as the estimated ULC for $x(0) = 0.05$ clearly illustrates.

By repeating the procedure over a range of the bifurcation parameter (c_3 in this case), the entire unstable branch of the bifurcation diagram can be estimated. Estimated bifurcation diagrams, obtained from perturbations of various amplitudes, are compared with the exact diagram in Fig. 2f. The estimation was interrupted if the trajectory converged to the stable limit cycle rather than the equilibrium, which happens if the initial condition is outside the ULC. Figure 2f shows the relatively good accuracy of the estimations. However, we note that the method cannot identify the fold bifurcation marking the end of the bistable range; in fact, the estimated branch of unstable solution continues to exists for $c_3 < c_3^*$, with rapidly increasing amplitude. This phenomenon is due to the slower dynamics (though not critically slow) characterizing the parameter space preceding the fold. Indeed, this effect is utilized in

[42,43] to predict the fold bifurcation itself. Nonetheless, this drawback of the algorithm is conservative concerning stability and, if properly accounted for, may be acceptable in real applications. In fact, ULCs estimated for parameter values where they do not exist typically exhibit large amplitudes, as demonstrated throughout the paper. Thus, in practice, an estimated ULC with a very large amplitude can be regarded as either practically irrelevant or a likely artifact of the estimation procedure. Additionally, as discussed in Sect. 3.2, the fold could be predicted if a more appropriate order of the interpolating polynomial were used.

3.2 Qualitative explanation

Topological considerations about the phase space and the critical slowing down imply that the logarithmic decrement curve intersects zero at the ULC. However, there is no inherent reason that a quadratic polynomial should accurately represent its trend. In fact, it is generally not the optimal estimator, as discussed below. In a simple single-DoF linear system with only a linear damping term, the logarithmic decrement remains constant. Conversely, the system studied above has three damping terms: linear, third-order, and fifth-order. It is expected that the third-order damping term introduces a quadratic trend in the logarithmic decrement, while the fifth-order term contributes a fourth-order trend. This can be understood intuitively, as in the system given by Eq. (2), the damping force is expressed as

$$F_\mathrm{d} = \left(c_1 - c_3\dot{x}^2 + c_3\dot{x}^4\right)\dot{x} = c\left(\dot{x}\right)\dot{x}, \tag{5}$$

with the logarithmic decrement being proportional to the damping coefficient. This hypothesis is validated by repeating the estimation from the previous section using a fourth-order polynomial.

Figure 3a, obtained for $c_3 = 0.6$, illustrates the logarithmic decrement estimation using either a quadratic (green), a fourth-order (black) or a sixth-order (red) polynomial. The initial conditions for the simulation were $x(0) = 0.1$ and $\dot{x}(0) = 0.001$. While the relative error for the quadratic order polynomial is 12.3 %, for the fourth-order polynomial it is only 3.5 %, which is a significant improvement. Conversely, increasing the polynomial to sixth order raises the error to 28.7 %. The errors refer to the estimated ULC amplitude for $\dot{x} = 0$.

Next, we consider $c_3 = 0.4$, for which no ULC exists. In this case, the initial conditions $x(0) = 0.3$ and $\dot{x}(0) = 0.001$ were utilized. As illustrated in Fig. 3b, the quadratic extrapolation still yields a ULC value. Since the logarithmic decrement points decrease with amplitude, even in the absence of ULCs, a quadratic extrapolation inevitably intersects the zero axis. In contrast, the fourth-order estimation produces a curve that does not intersect the zero axis, correctly indicating the absence of a ULC. In the figure, blue crosses indicate logarithmic decrement points from a separate simulation with larger initial conditions, which were not used in the estimation. The agreement between the fourth-order interpolation curve and those points is excellent; however, we note that the match deteriorates for smaller values of x_0.

Finally, Fig. 3c compares the bifurcation diagram's exact branch of unstable solutions with those estimated using quadratic and fourth-order polynomials. For the simulations, the initial conditions were $x(0) = 0.1$ and $\dot{x}(0) = 0.001$. The fourth-order extrapolation is significantly more accurate than the quadratic one; besides, it identifies the fold bifurcation, marked by the leftmost point presenting ULCs, with a relatively good accuracy.

Although these results clearly show that a quadratic polynomial is not the best choice for extrapolating logarithmic decrement points, it remains in use throughout the paper. In fact, when no information is available about the system's damping characteristics—which is often the case—a quadratic polynomial provides reasonably good results, as illustrated later, and avoids over-fitting, which can be detrimental for extrapolation.

3.3 Larger dimensional systems

For a single-DoF, two-dimensional system, implementing the ULC estimation method is significantly simpler compared to higher-dimensional systems. In a two-dimensional system, the so-called primary spectral submanifold [44,45] coincides exactly with the full phase space. Therefore, after any perturbation, the system remains on the primary spectral submanifold and converges in a spiral motion toward the equilibrium—unless the perturbation pushes it outside the ULC.

This is no longer valid for larger dimensional systems, leading to various challenges. First, a perturbation might move the system to a phase space region far

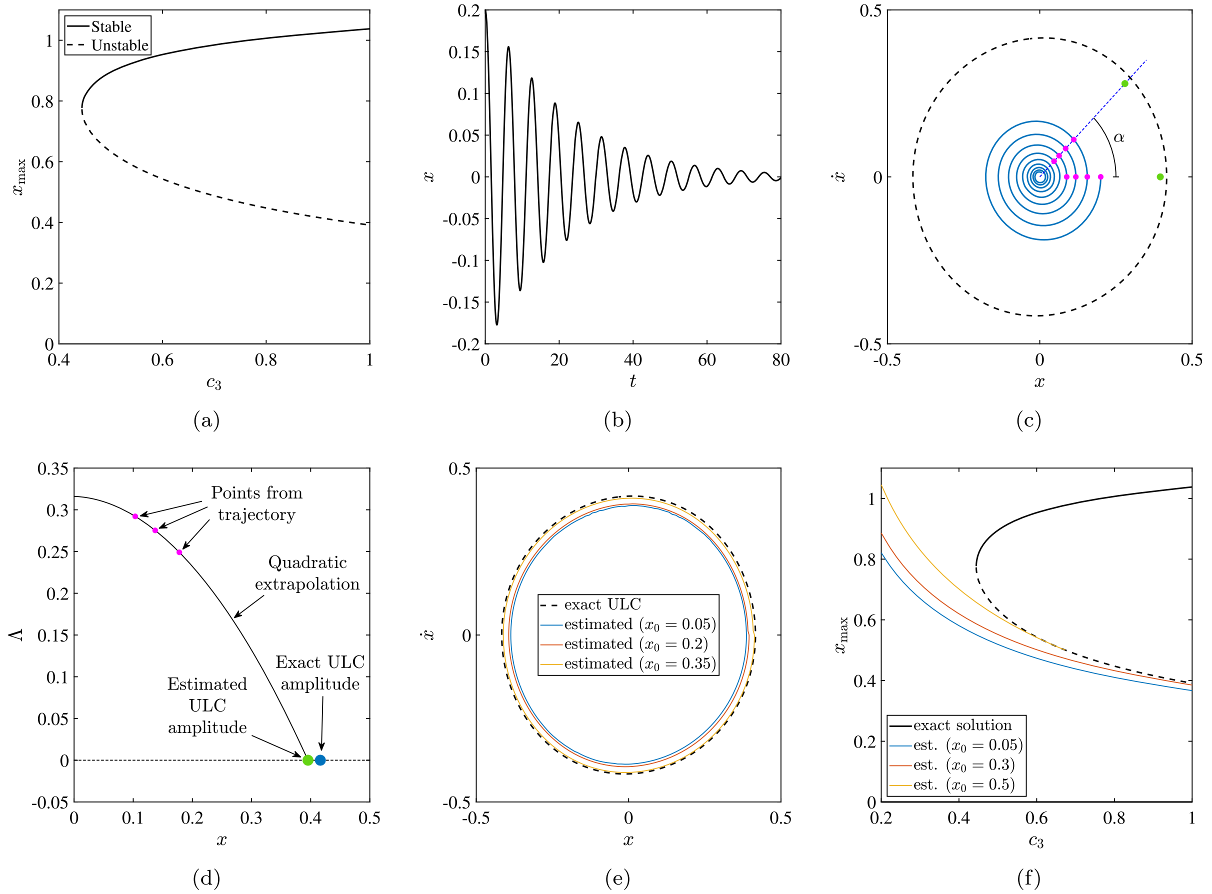

Fig. 2 **a** Bifurcation diagram for the system in Eq. (2), $c_1 = 0.1$. **b** Time series for the ULC estimation, obtained for $c_3 = 0.9$. **c** Phase portrait of the system for $c_3 = 0.9$; blue curve: simulated trajectory; black dashed curve: exact ULC; blue dashed line: Poincaré section; magenta dots: points of the trajectory selected for the ULC estimation; green dot: estimated ULC for either $\dot{x} = 0$ and on the Poincaré section. **d** Logarithmic decrement point and ULC estimation. **e** Comparison between exact and estimated ULC for different initial conditions. **f** Comparison between the exact and estimated unstable branch of the bifurcation diagram for different initial conditions. (Color figure online)

from the ULC, from which the system might converge toward the equilibrium without approaching the ULC. Consequently, it may carry only minimal information about the ULC. Assuming that any perturbation can be applied to the system, there is no straightforward solution to this issue. However, dynamical systems generally tend to converge towards the primary spectral submanifold, which, for a vibrating system, is often a two-dimensional invariant surface. As explained later, this tendency organizes the dynamics, making ULC estimation feasible.

Another important challenge in systems with two or more DoF is the possibility of modal interaction and beating phenomena, which can significantly complicate the ULC estimation. Currently, we cannot provide any solution for this issue, which remains an open topic and limits the method to system having one dominant vibration mode. This limitation is planned to be addressed in future studies.

Despite these problems, the method is generally applicable to systems with dimensions greater than two, as demonstrated in Sects. 5 and 6. The following discussion outlines the main adjustments needed for analyzing systems beyond two dimensions.

It is assumed that a trajectory converges towards the primary spectral submanifold while approaching the equilibrium; therefore, presents a sort of ordered dynamics. Generally, the initial segment of the trajec-

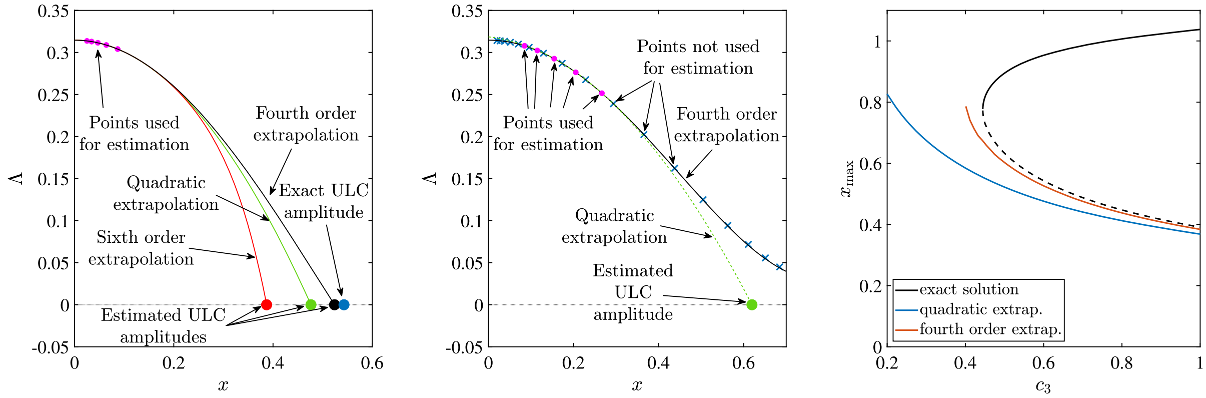

(a) (b) (c)

Fig. 3 **a** Logarithmic decrement points (magenta) and ULC amplitude estimation through quadratic (green), fourth- (black), and sixth-order (red) polynomial extrapolation, $c_3 = 0.6$ and $x_0 = 0.1$. **b** Logarithmic decrement points (magenta), ULC amplitude estimation with quadratic (green) and fourth-order polynomial extrapolation (black), blue crosses mark logarithmic decrement points not used for the estimation, $c_3 = 0.4$ and $x_0 = 0.3$. **c** Comparison between the bifurcation diagram's exact and estimated unstable branch with different order of polynomial extrapolation, $x_0 = 0.1$. (Color figure online)

tory is transient as it nears the spectral submanifold and should be discarded. The time length of this discarded segment cannot be defined a priory, since it depends on the initial conditions and on the system's characteristics.

One way to solve this problem is to estimate the ratio between the energy content of the first mode and that of the other modes. The signal is used for estimation only once this ratio exceeds a certain threshold. Several techniques can be applied for this purpose, such as a sliding-window FFT or wavelet transformation of the time series of one of the system coordinates, or through a sliding-window principal component analysis. A simpler approach is to discard a predefined initial portion of the trajectory, with the duration determined through visual inspection and refined using a trial-and-error method. For the cases considered here, the latter approach was used because it proved effective and significantly simpler.

For ULC prediction, each system coordinate is analyzed independently by projecting the trajectory onto a two-dimensional position-velocity subspace of the phase space. Poincaré sections are defined in this plane, and the prediction proceeds as in the single-DoF case. Since the analysis uses a projected trajectory, intersections may occur, potentially compromising the estimation. However, if a sufficiently long initial portion of the signal is disregarded and the system's topology is relatively simple, this problem is unlikely to arise. Alternatively, delay embedding could be used instead of a position-velocity subspace, which would also avoid the need for numerical differentiation of the position signal if velocity values are not directly available. Denoting the generic coordinate by x, the subspace would then be either $(x, \dot{x})$ or $(x(t), x(t-\tau))$.

If a mathematical model of the system is available, either from the system mechanics or obtained from data, modal coordinates can be used instead of the measured coordinates. However, since this method is designed specifically to avoid the need for a mathematical model, this scenario is not considered here.

For a single-DoF, two-dimensional system, only the first three logarithmic decrement/amplitude points are used to compute a quadratic interpolation, whose intersection with the zero axis indicates the estimated ULC amplitude. For larger dimensional systems, it is advisable to use more points and compute a least square approximation to determine the quadratic curve. In this way, the disturbance due to other modes potentially present in the signal is partially mitigated. The same approach should be applied to real systems to mitigate noise. However, the experimental validation of the method is beyond the scope of this paper and is left for future studies.

In the following sections, the method is applied to three inherently different systems, in order to assess its potential and limitations. Namely, a mass-on-moving-belt system exhibiting non-smooth behavior, a single-DoF model of turning machining described by a delayed differential equation (resulting in an infinite-dimensional system), and a two-DoF model of a pitch-and-plunge airfoil experiencing aeroelastic flutter.

4 Non-smooth system: mass-on-moving-belt

We analyze the mass-on-moving-belt system, depicted in Fig. 4a [14]. This archetypal model for friction-induced vibrations is commonly used to investigate the dynamics of violin strings [46] and brake squeal phenomena [47].

The system's dynamics is governed by the differential equation

$$\ddot{x} + 2\zeta\dot{x} + x = F_\mathrm{f}, \tag{6}$$

where time is non-dimensionalized by the oscillator natural frequency, ζ is the linear damping ratio and

$$\begin{cases} F_\mathrm{f} = \mu\left(v_\mathrm{rel}\right) & v_\mathrm{rel} \neq 0 \\ |F_\mathrm{f}| \leq \mu_\mathrm{s} & v_\mathrm{rel} = 0. \end{cases} \tag{7}$$

Following the Stribeck friction law [48], the friction coefficient μ is expressed as an exponentially decaying function:

$$\mu(v_\mathrm{rel}) = \left(\mu_\mathrm{d} + (\mu_\mathrm{s} - \mu_\mathrm{d})\,\mathrm{e}^{-\frac{|v_\mathrm{rel}|}{v_0}}\right)\mathrm{sign}\left(v_\mathrm{rel}\right), \tag{8}$$

where $v_\mathrm{rel} = v - \dot{x}$ denotes the relative velocity. The friction force exhibits a discontinuity at $v_\mathrm{rel} = 0$. Without loss of generality, the parameters are set to $\mu_\mathrm{s} = 1$, $\mu_\mathrm{d} = 0.5$, $v_0 = 0.5$, and $\zeta = 0.05$, as in [15].

The system's trivial solution is stable for large belt velocities v, while it undergoes a subcritical Andronov-Hopf bifurcation for $v = v_\mathrm{cr} = 1.151$, becoming unstable [14]. In correspondence of the stability loss, a branch of unstable periodic solutions emerges. For $v = 1.83$, this branch undergoes a non-smooth fold bifurcation, merging with another branch of stable periodic solutions, as depicted in Fig. 4b.

We apply the ULC estimation technique to this system. Since the system is two-dimensional, the procedure outlined in Sect. 3.1 can be directly implemented. However, the system's non-smooth nature may pose challenges for the estimation algorithm. We set $v = 1.6$ and we consider initial conditions $x(0) = x_0$ and $\dot{x}(0) = 0.001$. Initially, we choose $x_0 = 0.75$, which is approximately halfway between the ULC and the trivial equilibrium. The resulting time series is shown in Fig. 4c. Using the local maxima of the trajectory, we estimate the ULC amplitude as 1.665, while the exact amplitude is 1.539, resulting in an overestimation error of about 8 % (Fig. 4d and e). Repeating the procedure with different initial conditions, the error increases for lower initial conditions (12 % error for $x_0 = 0.5$) and decreases for larger initial conditions, closer to the ULC (4 % error for $x_0 = 1.0$ and about 1 % error for $x_0 = 1.25$), as shown in Fig. 4f. Overall, considering that the procedure's objective is to provide a rough estimation of the ULC, the result is satisfactory. We also note that the estimated ULC exhibits the same asymmetric shape as the exact ULC.

By repeating the same procedure for a range of values of the belt velocity v, i.e., the bifurcation parameter, the branch of ULCs can be estimated. The same perturbation amplitudes are considered, specifically $x_0 = 0.5$, 0.75, 1.0 and 1.25. As the ULC becomes larger, the estimation accuracy decreases because the trajectory is farther from the ULC. This behavior is confirmed by the results illustrated in Fig. 4b. Also in this case, the estimation algorithm fails to identify the saddle-node bifurcation, extending the estimated ULC branches into a region where no ULC exists. Additionally, unlike the previous case studied, no variation in the trend of the ULC branches is visible in the vicinity of the saddle-node bifurcation. This observation confirms the limitation of the method discussed above.

We note that, although this system is non-smooth, the non-smooth nature primarily impacts the stick–slip periodic solutions beyond the ULC; therefore, it only affects the estimation procedure marginally. Conversely, a strong non-smooth phenomenon acting between the trajectory and the ULC to be estimated would likely compromise the method's effectiveness completely.

5 System with time delay: turning machining

We consider a simplified model of a turning machine, as represented in Fig. 5a. The cutting tool is modeled as a single-DoF oscillator, where the mass, damping, and stiffness coefficients represent modal quantities, which are non-dimensionalized in this study. The workpiece, assumed stationary, interacts with the cutting tool through the cutting force F_c, which depends on

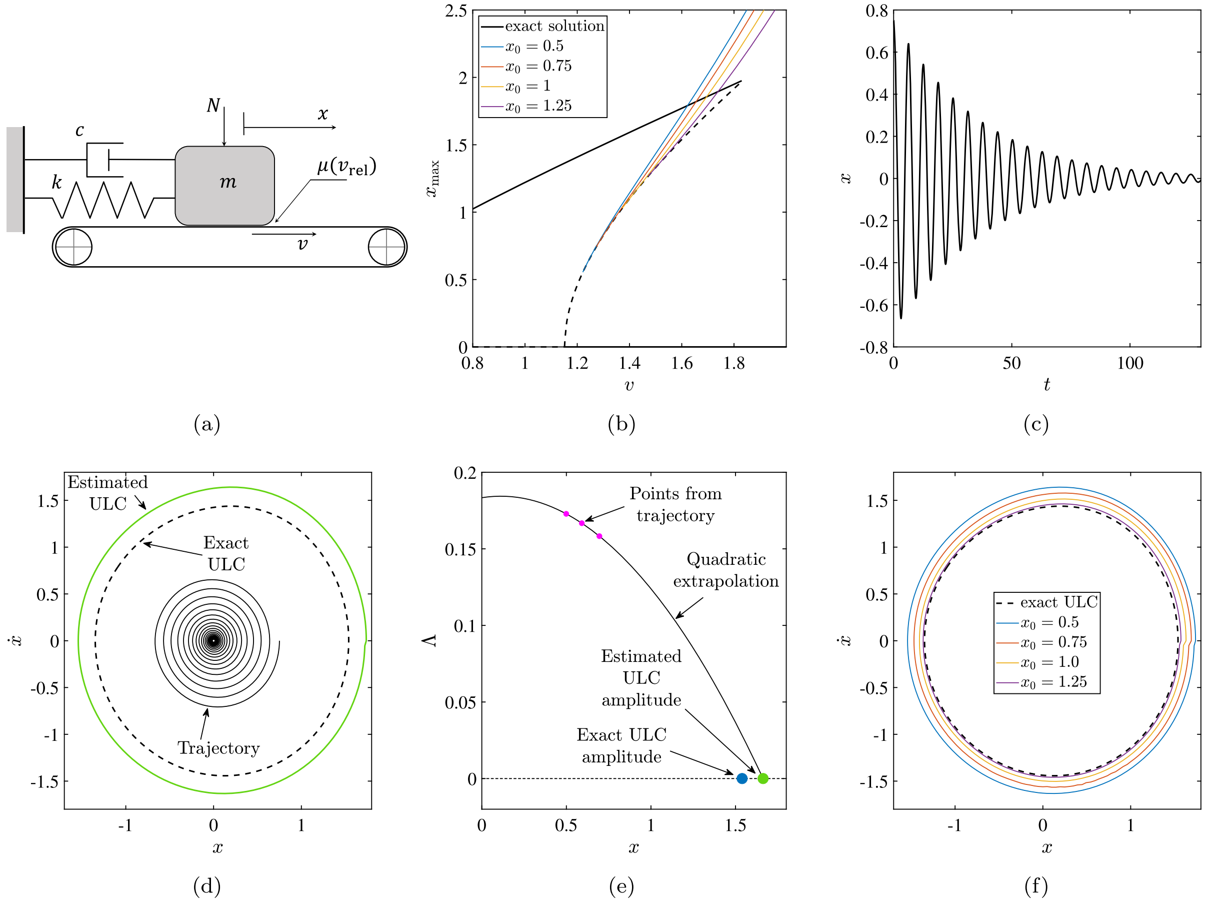

Fig. 4 Comprehensive results about the mass-on-belt system. **a** Mechanical model. **b** Bifurcation diagram; black lines: exact solution; colored lines: estimated. **c** Time series for the ULC estimation, obtained for $v = 1.6$. **d** Phase portrait of the system for $v = 1.6$; black dashed line: exact ULC; green solid line: estimated ULC. **e** Logarithmic decrement points and ULC estimation. **f** Comparison between exact and estimated ULC for different initial conditions. (Color figure online)

the depth of cut. The time-dependent depth of cut $h(t)$ results from the difference between the cutting tool's current position and its position one revolution earlier, introducing a time delay in the differential equation that describes the system's dynamics. Thus, the system is modeled by a delay differential equation.

The time delay in the equation of motion makes the system infinite-dimensional, despite having only one-DoF. Therefore, the system will be studied according to the methodology discussed in Sect. 3.3, as outlined below.

The depth of cut has nominal value h_0, which corresponds to the value it assumes in the steady cutting scenario. Calling x the modal displacement of the cutting tool's first mode, normalized by the nominal depth of cut, and normalizing time with respect to the cutting tool's first natural frequency, the equation of motion is

$$\begin{aligned}\ddot{x}(t) + 2\zeta\dot{x}(t) + x(t) &= p\big((x(t-\tau) - x(t)) \\ &\quad + \eta_2\,(x(t-\tau) - x(t))^2 + \eta_3\,(x(t-\tau) - x(t))^3\big),\end{aligned} \tag{9}$$

where ζ is the damping factor, τ is the dimensionless spindle period of rotation (and the dimensionless time delay of the system), p is the dimensionless chip width, and η_2 and η_3 characterize the nonlinearity of the cutting force function. In particular,

$$\begin{aligned}\eta_2 &= h_0\frac{\rho_2 + 3\rho_3 h_0}{\rho_1 + 2\rho_2 h_0 + 3\rho_3 h_0^2}\\ \eta_3 &= h_0^2\frac{\rho_3}{\rho_1 + 2\rho_2 h_0 + 3\rho_3 h_0^2},\end{aligned} \tag{10}$$

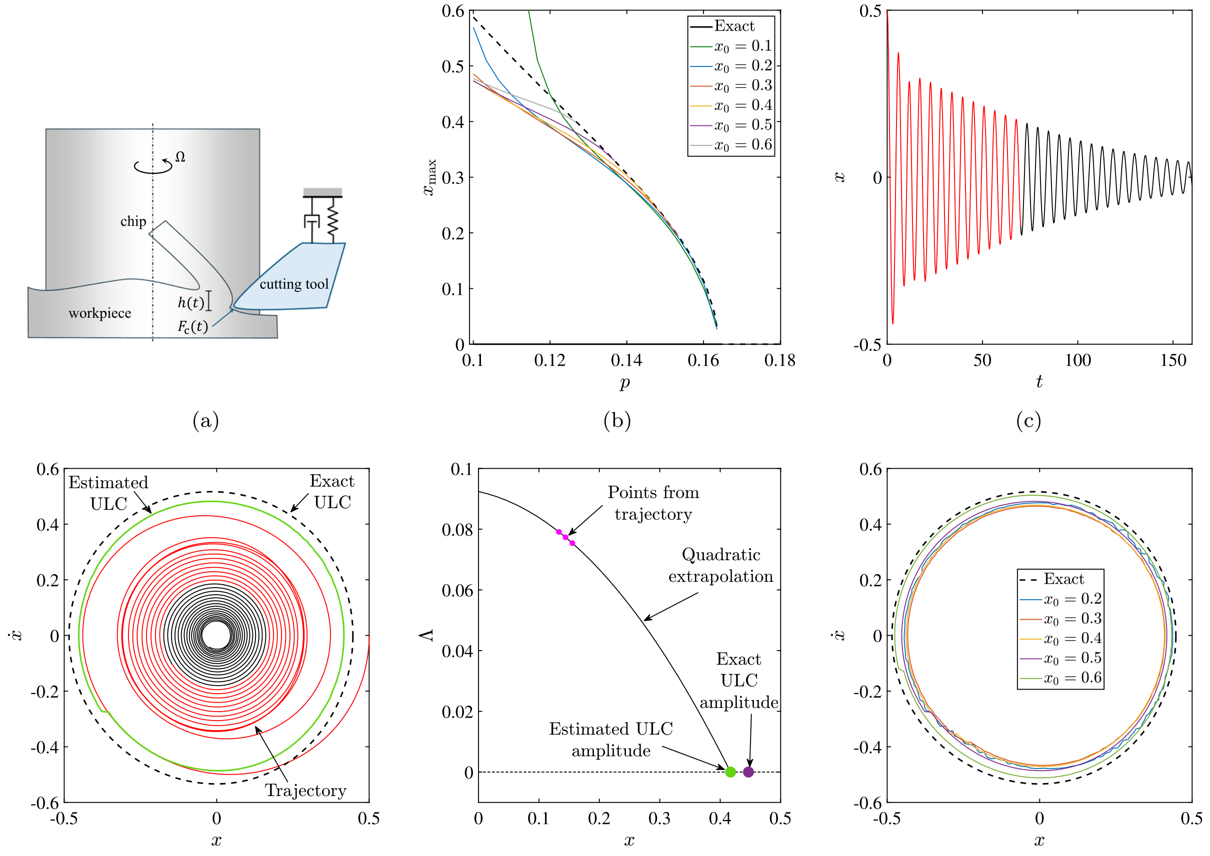

(a)
(b)
(c)
(d)
(e)
(f)

Fig. 5 Results for the turning machining model. **a** Mechanical model. **b** Bifurcation diagram; black dashed line: exact solution; colored solid lines: estimated. **c** Time series for ULC estimation obtained for $p = 0.12$; red line: discarded portion; black line: used portion. **d** Phase portrait of the system for $p = 0.12$; black dashed line: exact ULC; green solid line: estimated ULC; red (black) solid lines: discarder (used) portion of the trajectory. **e** Logarithmic decrement points and ULC estimation. **f** Comparison between exact and estimated ULC for different initial conditions for $p = 0.12$. (Color figure online)

where $\rho_1 = 6109.6\ \mathrm{Nmm}^{-2}$, $\rho_2 = -54141.6\ \mathrm{Nmm}^{-3}$ and $\rho_3 = 203769\ \mathrm{Nmm}^{-4}$ are coefficient identified experimentally in [49]. Although different models for the cutting force exist and their validity is an open research topic [50], they all agree on the nonlinear dependence of the cutting force on chip thickness. Without loss of generality, in this study, the coefficient values $\zeta = 0.05$, $\tau = 9$, $h_0 = 0.07$ mm are used. Further details about the adopted mathematical model can be found in [51]. The so-called fly-over effect [52], which occurs when the cutting tool momentarily leaves the work-piece, leading to a discontinuity in the cutting force, is not considered here. Since the model serves to demonstrate the method's effectiveness rather than to produce new insights into turning dynamics, this simplification is appropriate for the study's scope.

This system exhibits a classical subcritical Andronov-Hopf bifurcation, as illustrated in Fig. 5b. According to the mathematical model, no stable periodic solutions exist. However, in practice, large perturbations can induce periodic, quasiperiodic, or chaotic motions, often involving the fly-over effect [52]. The branch of ULCs extends until its amplitude surpasses the chip thickness, beyond which the mathematical model is no longer valid.

To generate time series, we use the following initial function:

$$\begin{aligned} &x(t) = 0,\ \dot{x}(t) = 0 \quad \text{for } t \in (-\tau, 0) \\ &x(t) = x_0,\ \dot{x}(t) = 0 \quad \text{for } t = 0. \end{aligned} \tag{11}$$

Initially, we set $p = 0.12$. For this p value, trajectories converge to the equilibrium for $x_0 < 0.6986$; otherwise, they diverge.

The ULC is initially estimated for $x_0 = 0.5$. Due to the infinite-dimensional nature of the system, we discard the first 70 time units of the time series to allow the system to converge to the vicinity of the primary spectral submanifold. The length of the discarded portion of the time series was determined through a trial-and-error process. Slightly adjusting this length does not significantly alter the estimation outcome.

The obtained time series is illustrated in Fig. 5c, where the red curve represents the discarded segment of the time series, while only the black part is used for the estimation. The trajectory is represented in the phase space in Fig. 5d. The estimated ULC, represented in green in Fig. 5d, closely approximates the exact ULC depicted by the black dashed curve with a relative error of approximately 6.6 % at $\dot{x} = 0$. We note that, although the red part of the trajectory is relatively close to the ULC and cannot be considered a small perturbation, the black part is relatively far from the ULC.

Figure 5e shows the logarithmic decrement-amplitude points extracted from the trajectory at $\dot{x} = 0$. The difference between the exact and the estimated ULC amplitude, derived from the quadratic extrapolation, is visible in the figure.

The procedure is further validated utilizing different initial conditions, down to $x_0 = 0.2$. The relative error obtained for the different cases (computed at $\dot{x} = 0$) is 2.3 % for $x_0 = 0.2$, 8.1 % for $x_0 = 0.3$, 8.4 % for $x_0 = 0.4$, and 3.1 % for $x_0 = 0.6$. Interestingly, in this case larger initial conditions do not necessarily reduce the error.

Finally, Fig. 5b compares the estimated ULC branches, derived from different perturbation levels, with the exact one. All branches provide an acceptable estimation, except for $x_0 = 0.1$, which predicts excessively large amplitudes for $p < 0.115$. Unsurprisingly, the accuracy of the estimation decreases as the ULC moves farther from the trajectory used for estimation.

6 Multi-DoF system: aeroelastic flutter

The method is applied to a pitch-and-plunge airfoil undergoing flutter oscillations (Fig. 6). Variants of the pitch-and-plunge wing model have been used in several previous studies [53–56], differing only slightly in the system's nonlinearities compared to the model employed here. The model has two DoFs, making it four-dimensional; thus, the analysis follows the method outlined in Sect. 3.3.

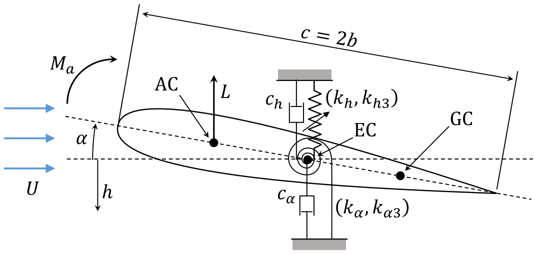

Fig. 6 Mechanical model of the pitch-and-plunge airfoil

The system dynamics is governed by the following system of non-dimensional differential equations:

$$\mathbf{M}\ddot{\mathbf{x}} + \mathbf{C}\dot{\mathbf{x}} + \mathbf{K}\mathbf{x} + \mathbf{b}\left(\mathbf{x}\right) = \mathbf{0}, \tag{12}$$

where

$$\begin{aligned} &\mathbf{x} = \begin{bmatrix} y \\ \alpha \end{bmatrix}, \ \mathbf{K} = \begin{bmatrix} \Omega^2 & \beta u^2 \\ 0 & r_\alpha^2 - \nu u^2 \end{bmatrix}, \ \mathbf{C} = \begin{bmatrix} \zeta_\mathrm{h} + \beta u & 0 \\ -\nu u & \zeta_\alpha \end{bmatrix}, \\ &\mathbf{M} = \begin{bmatrix} 1 & x_\alpha \\ x_\alpha & r_\alpha^2 \end{bmatrix}, \ \mathbf{b} = \begin{bmatrix} 0 \\ \xi_{\alpha 3}\alpha^3 + \xi_{\alpha 5}\alpha^5 \end{bmatrix}, \end{aligned} \tag{13}$$

y marks the heave displacement, non-dimensionalized by the semichord of the airfoil, α indicates the pitch rotation, while u depicts the non-dimensional flow velocity. Details on the physical meaning of remaining parameters can be found in [4], where a similar notation is used for ease of comparison. The adopted parameter values are $r_\alpha = 0.5$, $x_\alpha = 0.2$, $\nu = 0.08$, $\beta = 0.2$, $\Omega = 0.5$, $\zeta_\mathrm{h} = 0.01$, $\zeta_\alpha = 0.01$, $\xi_{\alpha 3} = -1$, and $\xi_{\alpha 5} = 20$.

Figure 7a shows the system bifurcation diagram for variations of the flow velocity u. The equilibrium loses stability via a subcritical Andronov-Hopf bifurcation, giving rise to a branch of unstable periodic solutions that reverse direction at a fold for $u = u^*$, becoming stable. The Andronov-Hopf bifurcation occurs at $u = 0.933$, while the fold is located at $u = u^* = 0.911$.

We proceed to estimate the ULC for $u = 0.92$. A trajectory is simulated with initial conditions $y(0) = 0$, $\alpha(0) = \alpha_0$, $\dot{y}(0) = 0$, and $\dot{\alpha}(0) = 0$. For the first trial, we set $\alpha_0 = 0.05$. The obtained time series is illustrated in Fig. 7b, while the corresponding trajectory in the phase space is shown in Fig. 7c and d in two different projections. The trajectory is represented by both the red and black curves in the figures; however, the red curve indicates the discarded segment, while the black curve is used for the analysis. Also in this case, the length of the discarded segment was determined through a trial-and-error procedure and was set to 65 time instant. We note that the estimation was robust to variations in the length of the discarded segment.

Following the procedure in Sect. 3.3, we first consider the plunge motion y and its derivative $\dot{y}$. The estimation results are illustrated in Fig. 7c, where the black dashed line indicates the exact ULC, while the green line the estimated one. The agreement between the two is excellent, with a relative error for $\dot{y} = 0$ of only 3.1 %. Figure 7d presents the results concerning the pitch DoF α. In this case, the estimation is slightly less accurate but sufficiently good for the purposes of the proposed methodology, with a relative error of 5.1 %.

Figure 7e illustrates the estimated logarithmic decrement relative to the peaks of the pitch displacement. The figure compares the estimated ULC amplitude (green dot) and the exact value (blue dot). We note that in this case, 11 logarithmic decrement-amplitude points are used to mitigate disturbances generated by the system's second vibration mode. The quadratic curve was obtained using a least square approximation.

Figure 7f shows the results obtained with different initial conditions (in the α-$\dot{\alpha}$ space). All tested cases yield satisfactory results. The obtained relative errors are 6 % for $\alpha_0 = 0.03$, 3.7 % for $\alpha_0 = 0.07$, and 0.7 % for $\alpha_0 = 0.1$.

Finally, the colored curves in Fig. 7a mark the estimated bifurcation diagram for the four considered initial conditions of the signals. In all cases, the estimation remains accurate up to the fold bifurcation, where differences between the four cases are practically negligible. The algorithm does not detect that, prior to the fold, no ULC exists, highlighting a previously discussed limitation.

7 Discussion and conclusions

This study introduced a new method for estimating unstable limit cycles (ULCs) around stable equilibrium solutions. The method leverages the critical slowing down of the system dynamics near a steady-state solution, whether stable or unstable. By recognizing that the logarithmic decrement effectively measures this slowing down, the method allows for the estimation of a ULC from a trajectory initiated by a small perturbation from equilibrium.

The method was tested on various systems, each presenting different challenges. Apart from a relatively simple case of a resonator with nonlinear damping, we investigated the mass-on-moving-belt system, which features non-smoothness, a turning machining model with a time-delay equation of motion, and a pitch-and-plunge airfoil undergoing flutter, which has two-DoF (unlike the other systems with only one DoF). The method proved effective in all cases.

The main advantages of the method are:

- It requires only a single time series for the estimation, making it significantly more computationally efficient than most data-driven methods and easily implementable in experimental systems.
- The algorithm does not require any sort of mathematical model of the system. This offers a major advantage over other data-driven methods, which usually have predictive properties only through an estimated mathematical model, either physics-based or black-box. By eliminating the need for model generation and interpretation, some potential sources of error are avoided and computational cost is significantly reduced.
- Implementing the method in real systems does not require actuators or feedback controllers. Other experimental methods for identifying unstable solutions often depend on feedback control, like the control-based optimization method [57], or at least on actuators [32]. The method developed in this study might be effective even when utilizing only natural perturbations that the system experiences during normal operation.
- The method does not require the system's dynamics to be in close proximity to the ULC, but it estimates its position from a certain distance in the phase space. However, the accuracy of the estimation improves as the dynamics approach the ULC.

Regarding the limitations of the method, we note:

- The method relies on quadratic regression to estimate the ULC amplitude. However, there is no guarantee that the logarithmic decrement follows a quadratic trend, as this is not generally true. While this may introduce some error, the approximation has proven to be a simple yet effective balance between computational simplicity and precision. We note that tests performed with a linear regression provided poor results (not shown here), while higher order polynomial might generate large

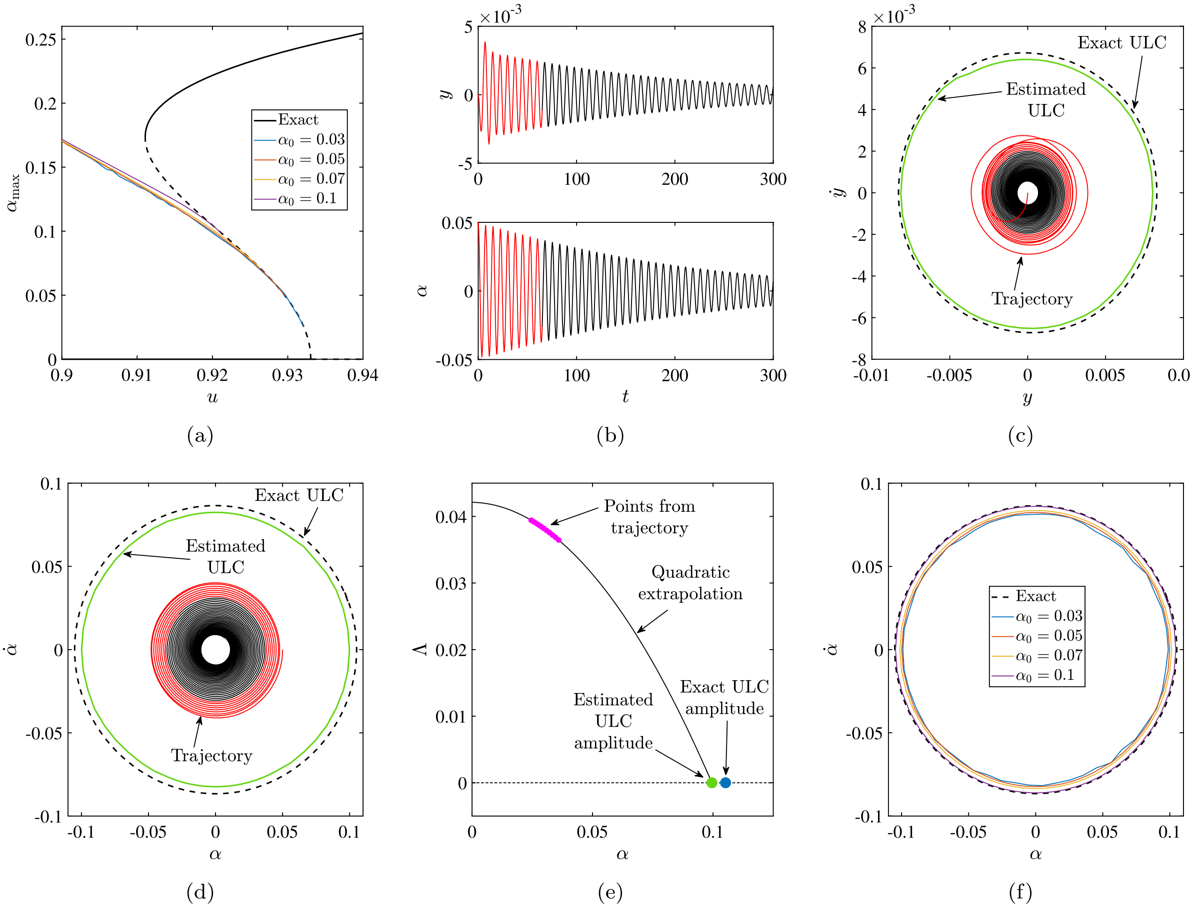

(a) (b) (c)

(d) (e) (f)

Fig. 7 Results about the pitch-and-plunge wing profile system. **a** Bifurcation diagram. **b** Time series for the ULC estimation, obtained for $u = 0.92$; red line: discarded portion; black line: used portion. **c**,**d** Phase portrait of the system for $u = 0.92$ (y and α coordinates, respectively); red line: discarded portion; black line: used portion; black dashed line: exact ULC; green solid line: estimated ULC. **e** Logarithmic decrement points and ULC estimation. **f** Comparison between exact and estimated ULC for different initial conditions. (Color figure online)

error in the presence of noise because of overfitting. Nevertheless, the optimal polynomial order is system-dependent, and in some cases a higher or lower order polynomial might be more effective. For example, in the presence of high noise, a linear regression might outperform a quadratic one, while a third order polynomial might avoid the false identification of a non-existent ULC near a fold bifurcation. In this context, if some information about the possible order of the system nonlinearities is available, for example through the sparse identification of nonlinear dynamics method [58,59], it can be used for choosing a more appropriate regression algorithm, including non-polynomial curves.

- If the phenomenon generating the ULC is triggered beyond a certain oscillation amplitude and it does not exist below this amplitude—as typical for discontinuous or non-smooth systems—the method will fail for perturbations smaller than this amplitude, because the generated trajectories contain no information about the ULC. However, as demonstrated in Sect. 4, in general, non-smoothness does not necessarily preclude the method from functioning.
- In its present form, the method cannot address systems exhibiting strong modal interaction because the exchange of energy between the modes would make the energy decrement irregular.

- Multi-DoF systems pose a significant challenge to the methods, as typical for global analysis techniques. The application of the method to such systems requires discarding the initial part of the signal. Nevertheless, the sensitivity of the method to the discarded portion is not critical, and the method worked effectively for both a single-DoF infinite-dimensional system (Sect. 5) and a two-DoF one (Sect. 6). In future studies, an objective metric to define the portion of the trajectory to be discarded should be developed to reduce the algorithm's dependence on user discretion. Additionally, more challenging tests should be performed to assess the algorithm's performance for multi-DoF systems.
- The method makes specific assumptions while extrapolating information from a trajectory. As a result, it may produce wrong results if the system exhibits unusual dynamical behavior, related, for examples, to a twisted primary spectral submanifold [60]. Therefore, users should be aware that the estimated ULC might be significantly incorrect in such cases.

As expected, and confirmed by the obtained results, in general, the closer the initial condition is to the unstable solution, the better the approximation. For systems whose initial conditions can be freely chosen, this property can be exploited by iteratively generating multiple trajectories, with initial conditions set on the ULC estimated in the previous iteration. This approach could yield a highly accurate estimation in just a few iteration steps.

Other future developments of this work include an experimental validation of the method to confirm its applicability to real-world scenarios. Specifically, its effectiveness in the presence of noise and unmeasured DoF will be assessed. Additionally, the method will be extended to identify ULCs in topologically different phase portraits, for example where the ULC does not necessarily surround a stable equilibrium, or in non-autonomous systems. Finally, efforts will focus on developing a strategy to extract useful information from the portion of the signal that is discarded in multi-DoF systems.

Acknowledgements The author thanks Bence Szaksz and Balázs Bauer for extensive discussions.

Funding The research reported in this paper has been supported by Project no. TKP-6-6/PALY-2021 provided by the Ministry of Culture and Innovation of Hungary from the National Research, Development and Innovation Fund, financed under the TKP2021-NVA funding scheme and by the National Research, Development and Innovation Office (Grant no. NKFI-134496).

Data Availability Statement Not applicable.

Code availability The code utilized for generating the presented results is publicly available at https://gdrg.mm.bme.hu.

Declarations

Conflict of interest The author declares that he has no Conflict of interest.

References

1. Dombovari, Z., Stepan, G.: On the bistable zone of milling processes. Philos. Trans. R. Soc. A: Math., Phys. Eng. Sci. **373**(2051), 20140409 (2015)
2. Dombovari, Z., Iglesias, A., Molnar, T.G., Habib, G., Munoa, J., Kuske, R., Stepan, G.: Experimental observations on unsafe zones in milling processes. Phil. Trans. R. Soc. A **377**(2153), 20180125 (2019)
3. Dimitriadis, G., Li, J.: Bifurcation behavior of airfoil undergoing stall flutter oscillations in low-speed wind tunnel. AIAA J. **47**(11), 2577–2596 (2009)
4. Malher, A., Touzé, C., Doaré, O., Habib, G., Kerschen, G.: Flutter control of a two-degrees-of-freedom airfoil using a nonlinear tuned vibration absorber. J. Comput. Nonlinear Dyn. **12**(5), 051016 (2017)
5. Cherubini, S.: Unraveling transition and turbulence using nonlinear optimization. In: IUTAM Laminar-Turbulent Transition: 9th IUTAM Symposium, London, UK, September 2–6, 2019, pp. 3–18. Springer (2022)
6. Nagy, P.T., Kulcsár, M.: Predicting the energy stability limit of shear flows using weighted velocity components. Physics of Fluids **35**(10) (2023)
7. Kadar, F., Stepan, G.: Nonlinear dynamics and safety aspects of pressure relief valves. Nonlinear Dyn. **111**(13), 12017–12032 (2023)

8. Beregi, S., Takacs, D., Stepan, G.: Bifurcation analysis of wheel shimmy with non-smooth effects and time delay in the tyre-ground contact. Nonlinear Dyn. **98**(1), 841–858 (2019)
9. Habib, G., Epasto, A.: Towed wheel shimmy suppression through a nonlinear tuned vibration absorber. Nonlinear Dyn. **111**(10), 8973–8986 (2023)
10. Horvath, H.Z., Takacs, D.: Stability and local bifurcation analyses of two-wheeled trailers considering the nonlinear coupling between lateral and vertical motions. Nonlinear Dynamics pp. 1–18 (2022)
11. Ubellacker, W., Csomay-Shanklin, N., Molnar, T.G., Ames, A.D.: Verifying safe transitions between dynamic motion primitives on legged robots. In: 2021 IEEE/RSJ International Conference on Intelligent Robots and Systems (IROS), pp. 8477–8484. IEEE (2021)
12. Habib, G., Bártfai, A., Barrios, A., Dombovari, Z.: Bistability and delayed acceleration feedback control analytical study of collocated and non-collocated cases. Nonlinear Dyn. **108**(3), 2075–2096 (2022)
13. Bartfai, A., Dombovari, Z.: HOPF bifurcation calculation in neutral delay differential equations: nonlinear robotic arms subject to delayed acceleration feedback control. Int. J. Non-Linear Mech. **147**, 104239 (2022)
14. Papangelo, A., Ciavarella, M., Hoffmann, N.: Subcritical bifurcation in a self-excited single-degree-of-freedom system with velocity weakening-strengthening friction law: analytical results and comparison with experiments. Nonlinear Dyn. **90**, 2037–2046 (2017)
15. Hu, J.L., Habib, G.: Friction-induced vibration suppression via the tuned mass damper: optimal tuning strategy. Lubricants **8**(11), 100 (2020)
16. Orosz, G., Wilson, R.E., Stépán, G.: Traffic Jams: dynamics and control. Philos. Trans. R. Soc. A: Math., Phys. Eng. Sci. **368**(1928), 4455–4479 (2010)
17. Kiss, A.K., Avedisov, S.S., Bachrathy, D., Orosz, G.: On the global dynamics of connected vehicle systems. Nonlinear Dyn. **96**, 1865–1877 (2019)
18. Pourbeik, P., Kundur, P.S., Taylor, C.W.: The anatomy of a power grid blackout-root causes and dynamics of recent major blackouts. IEEE Power Energ. Mag. **4**(5), 22–29 (2006)
19. Gajduk, A., Todorovski, M., Kocarev, L.: Stability of power grids: an overview. Eur. Phys. J. Spec. Top. **223**(12), 2387–2409 (2014)
20. Hsu, C.S.: Cell-to-cell mapping: a method of global analysis for nonlinear systems, vol. 64. Springer Science & Business Media, Berlin (2013)
21. Papachristodoulou, A., Prajna, S.: On the construction of lyapunov functions using the sum of squares decomposition. In: Proceedings of the 41st IEEE Conference on Decision and Control, 2002., **3**, 3482–3487. IEEE (2002)
22. Habib, G.: Dynamical integrity assessment of stable equilibria: a new rapid iterative procedure. Nonlinear Dyn. **106**(3), 2073–2096 (2021)
23. Szaksz, B., Stepan, G., Habib, G.: Dynamical integrity estimation in time delayed systems: a rapid iterative algorithm. J. Sound Vib. **571**, 118045 (2024)
24. Virgin, L.N.: Introduction to experimental nonlinear dynamics: a case study in mechanical vibration. Cambridge University Press, Cambridge (2000)
25. Waite, J., Virgin, L.N., Wiebe, R.: Competing responses in a discrete mechanical system. Int. J. Bifurc Chaos **24**(01), 1430003 (2014)
26. Zakynthinaki, M.S., Stirling, J.R., Cordente Martínez, C.A., Díaz de Durana, A.L., Quintana, M.S., Romo, G.R., Molinuevo, J.S.: Modeling the basin of attraction as a two-dimensional manifold from experimental data: applications to balance in humans. Chaos: Interdiscip. J. Nonlinear Sci. **20**(1), 013119 (2010)
27. Habib, G., Cirillo, G.I., Kerschen, G.: Isolated resonances and nonlinear damping. Nonlinear Dyn. **93**(3), 979–994 (2018)
28. Nayfeh, A.H., Balachandran, B.: Applied Nonlinear Dynamics: Analytical, Computational, and Experimental Methods. Wiley, Hoboken (2008)
29. Sieber, J., Krauskopf, B.: Control based bifurcation analysis for experiments. Nonlinear Dyn. **51**(3), 365–377 (2008)
30. Barton, D.A., Sieber, J.: Systematic experimental exploration of bifurcations with noninvasive control. Phys. Rev. E-Stat., Nonlinear, Soft Matter Phys. **87**(5), 052916 (2013)
31. Peter, S., Leine, R.I.: Excitation power quantities in phase resonance testing of nonlinear systems with phase-locked-loop excitation. Mech. Syst. Signal Process. **96**, 139–158 (2017)
32. Raze, G., Abeloos, G., Kerschen, G.: Experimental continuation in nonlinear dynamics: recent advances and future challenges. Under review (2024)
33. Schwarz, S., Kohlmann, L., Hartung, A., Gross, J., Scheel, M., Krack, M.: Validation of a turbine blade component test with frictional contacts by phase-locked-loop and force-controlled measurements. J. Eng. Gas Turbines Power **142**(5), 051006 (2020)
34. Strogatz, S.H.: Nonlinear Dynamics and Chaos with Student Solutions Manual: With Applications to Physics, Biology, Chemistry, and Engineering. CRC Press, Boca Raton (2018)
35. Lim, J., Epureanu, B.I.: Forecasting a class of bifurcations: theory and experiment. Phys. Rev. E **83**(1), 016203 (2011)
36. Ghadami, A., Epureanu, B.I.: Bifurcation forecasting for large dimensional oscillatory systems: forecasting flutter using gust responses. J. Comput. Nonlinear Dyn. **11**(6), 061009 (2016)
37. Yamasaki, H., Epureanu, B.I.: Forecasting supercritical and subcritical HOPF bifurcations in aeroelastic systems. Int. J. Non-Linear Mech. **94**, 400–405 (2017)
38. Riso, C., Ghadami, A., Cesnik, C.E., Epureanu, B.I.: Data-driven forecasting of postflutter responses of geometrically nonlinear wings. AIAA J. **58**(6), 2726–2736 (2020)
39. García Pérez, J., Ghadami, A., Sanches, L., Epureanu, B.I., Michon, G.: Data-driven bifurcation analysis of experimental aeroelastic systems using preflutter measurements. AIAA J. **62**(5), 1906–1914 (2024)
40. Chen, S., Epureanu, B.: Forecasting bifurcations in parametrically excited systems. Nonlinear Dyn. **91**, 443–457 (2018)
41. Ghadami, A., Epureanu, B.I.: Forecasting the onset of traffic congestions on circular roads. IEEE Trans. Intell. Transp. Syst. **22**(2), 1196–1205 (2020)
42. Habib, G.: Predicting saddle-node bifurcations using transient dynamics: a model-free approach. Nonlinear Dyn. **111**(22), 20579–20596 (2023)
43. Kadar, F., Stepan, G., Habib, G.: Model-free fold bifurcation prediction from pre-bifurcation scenario: experimen-

tal validation through wheel shimmy vibrations. Nonlienar Dynamics (2025)
44. Haller, G., Ponsioen, S.: Nonlinear normal modes and spectral submanifolds: existence, uniqueness and use in model reduction. Nonlinear Dyn. **86**, 1493–1534 (2016)
45. Cenedese, M., Axås, J., Bäuerlein, B., Avila, K., Haller, G.: Data-driven modeling and prediction of non-linearizable dynamics via spectral submanifolds. Nat. Commun. **13**(1), 872 (2022)
46. Leine, R., Van Campen, D., De Kraker, A., Van Den Steen, L.: Stick-slip vibrations induced by alternate friction models. Nonlinear Dyn. **16**, 41–54 (1998)
47. Hetzler, H., Schwarzer, D., Seemann, W.: Steady-state stability and bifurcations of friction oscillators due to velocity-dependent friction characteristics. Proc. Inst. Mech. Eng., Part K: J. Multi-body Dyn. **221**(3), 401–412 (2007)
48. Jackobson, B.: The stribeck memorial lecture. Tribol. Int. **36**(11), 781–789 (2003)
49. Shi, H., Tobias, S.: Theory of finite amplitude machine tool instability. Int. J. Mach. Tool Des. Res. **24**(1), 45–69 (1984)
50. Dombovari, Z., Wilson, R.E., Stepan, G.: Estimates of the bistable region in metal cutting. Proc. R. Soc. A: Math. Phys. Eng. Sci. **464**(2100), 3255–3271 (2008)
51. Habib, G., Kerschen, G., Stepan, G.: Chatter mitigation using the nonlinear tuned vibration absorber. Int. J. Non-Linear Mech. **91**, 103–112 (2017)
52. Beri, B., Stepan, G.: Essential chaotic dynamics of chatter in turning processes. Chaos: Interdiscip. J. Nonlinear Sci. (2020)
53. Dowell, E.H.: A modern course in aeroelasticity, vol. 217. Springer, Berlin (2014)
54. Lee, Y.S., Vakakis, A.F., Bergman, L.A., McFarland, D.M., Kerschen, G.: Suppressing aeroelastic instability using broadband passive targeted energy transfers, part 1: theory. AIAA J. **45**(3), 693–711 (2007)
55. Lee, Y.S., Kerschen, G., McFarland, D.M., Hill, W.J., Nichkawde, C., Strganac, T.W., Bergman, L.A., Vakakis, A.F.: Suppressing aeroelastic instability using broadband passive targeted energy transfers, part 2: experiments. AIAA J. **45**(10), 2391–2400 (2007)
56. Habib, G., Horváth, Á.: Fold bifurcation identification through scientific machine learning. Phys. D: Nonlinear Phenom. **472**, 134490 (2024)
57. Renson, L., Sieber, J., Barton, D.A., Shaw, A., Neild, S.: Numerical continuation in nonlinear experiments using local gaussian process regression. Nonlinear Dyn. **98**, 2811–2826 (2019)
58. Brunton, S.L., Proctor, J.L., Kutz, J.N.: Discovering governing equations from data by sparse identification of nonlinear dynamical systems. Proc. Natl. Acad. Sci. **113**(15), 3932–3937 (2016)
59. Naozuka, G.T., Rocha, H.L., Silva, R.S., Almeida, R.C.: Sindy-SA framework: enhancing nonlinear system identification with sensitivity analysis. Nonlinear Dyn. **110**(3), 2589–2609 (2022)
60. Stoychev, A.K., Römer, U.J.: Failing parametrizations: What can go wrong when approximating spectral submanifolds. Nonlinear Dyn. **111**(7), 5963–6000 (2023)